Combustion and Flame xxx (2014) xxx–xxx

Contents lists available at ScienceDirect

Combustion and Flame

journal homepage: www.elsevier.com/locate/combustflame

Experimental investigation of the inner structure of premixed turbulent methane/air flames in the thin reaction zones regime

Parsa Tamadonfar *, Ömer L. Gülder

Institute for Aerospace Studies, University of Toronto, 4925 Dufferin Street, Toronto, Ontario M3H 5T6, Canada

ARTICLE INFO

Article history:
Received 20 December 2013
Received in revised form 20 March 2014
Accepted 5 July 2014
Available online xxxx

Keywords:
Premixed turbulent combustion
Thin reaction zones regime
Flame front thickness

ABSTRACT

The thermal flame front thickness of premixed turbulent methane/air flames stabilized on a Bunsen-type burner was investigated experimentally. The instantaneous velocity and temperature fields were measured using the particle image velocimetry and Rayleigh scattering techniques, respectively. The Karlovitz number was varied from 1.2 to 20.7, indicating that the measured data are located within the thin reaction zones regime. The normalized preheat zone and reaction zone thicknesses decreased with increasing non-dimensional turbulence intensity in ultra-lean premixed turbulent flames under a constant equivalence ratio of 0.6, whereas they increased with increasing equivalence ratios from 0.6 to 1.0 under a constant bulk flow velocity. These normalized thicknesses were higher than unity for equivalence ratios ranging from 0.8 to 1.0, indicating that the internal structure of the flame fronts deviates from the thin laminar flamelet assumption. However, the mean widening for progress variable contours of premixed turbulent flames in comparison with corresponding values of unstrained premixed laminar flames was insignificant, implying that the influence of turbulent eddies on the flame front broadening is negligible. The normalized preheat zone and reaction zone thicknesses showed no overall trend with increasing non-dimensional longitudinal integral length scale. The normalized preheat zone and reaction zone thicknesses decreased by increasing the Karlovitz number, suggesting that increasing the total stretch rate is the controlling mechanism in the reduction of flame front thickness for the experimental conditions studied in this work. The probability density functions of the progress variable in front of the preheat layers were found to be insensitive to an increase in the non-dimensional turbulence intensity.

1. Introduction

The chemical and hydrodynamic structures of a stretched premixed laminar flame are believed to be preserved in premixed turbulent flames over a range of conditions recognized as the flamelet regime [1]. Poinsot et al. [2] reported the existence of flamelet regime beyond the Klimov–Williams criterion using two-dimensional DNS. Later, Peters [3] extended the flamelet limit of premixed turbulent combustion by introducing the thin reaction zones regime in which the Kolmogorov-scaled structures are believed to be able to enter the preheat zone and distort the inner structure of the flame front significantly, while these structures are not capable to penetrate inside the thin reaction zone.

In his formulation of an expression for burning rates at high Karlovitz numbers, Zimont [4] assumed the presence of a thick reaction zone as compared to the flame front thickness at lower turbulence intensities. Ronney and Yakhot [5] argued that scales of turbulence smaller than the laminar flame front thickness at high turbulence intensity will increase both the flame front thickness and burning rate, that is, the flame will be broadened and accelerated by the smaller scales. They further indicated that as the Karlovitz number (Ka) increases, the flame front thickness is expected to increase. Mansour et al. [6] showed that the preheat zone thickness of a stoichiometric methane/air flame at $Ka = 91$ varies from 2 to 3.5 mm on a Bunsen-type burner, and the ratios of these thicknesses to the preheat zone thickness of the corresponding unstrained premixed laminar flame are larger than unity. Flame front thickening of lean propane/air flames stabilized on Bunsen-type and swirl burners for $2.7 < Ka < 11$ was reported by O'Young and Bilger [7]. Sankaran et al. [8] observed the broadening of the preheat zone of a lean preheated methane/air flame on a slot-burner flame using three-dimensional DNS, and claimed that the turbulent structures are the mechanism behind the flame front widening. Yuen and Gülder [9] investigated the variation of the thermal flame front thickness as a function of the non-dimensional turbulence intensity for methane/air and propane/air flames

* Corresponding author.
E-mail addresses: tamadonfar@utias.utoronto.ca, parsa.tamadonfar@utoronto.ca (P. Tamadonfar).

http://dx.doi.org/10.1016/j.combustflame.2014.07.001
0010-2180/

stabilized on a Bunsen-type burner for $1.1 < Ka < 37.7$ and $0.8 < Ka < 23.3$, respectively, without considering any influence the equivalence ratio might have. They have concluded that the thermal flame front thickness gets thicker with increasing non-dimensional turbulence intensity for both methane/air and propane/air flames. Driscoll [10] argued that the formation of thick flame fronts cannot be inferred with the penetration of turbulent structures into the flame fronts, and concluded that other possibilities such as the misalignment of the laser to the flame layers or the effect of strain rate on the flame front may be the mechanisms behind the formation of thick flame fronts.

On the other hand, Buschmann et al. [11] observed that the mean flame front thickness is considerably thinner than the corresponding value of the unstrained premixed laminar flame for methane/air flames stabilized on a Bunsen-type burner for $1 < Ka < 13.6$. Soika et al. [12] reported the existence of a thin flame front thickness for methane/air V-shaped flames for $0.1 < Ka < 4.6$. Most et al. [13] reported significant thinning of the flame front thickness for lean methane/air flames stabilized on a bluff-body by systematically increasing the bulk flow velocity. de Goey et al. [14] reported a similar trend when the Karlovitz number was increased from 0.98 to 12.5 on a weak-swirl burner, and confirmed their observation by numerical and theoretical analysis. Three-dimensional DNS calculations for rich turbulent methane/air expanding flames at relatively high Karlovitz numbers showed a decreasing trend in the flame front thickness with increasing the turbulent Reynolds number [15]. Based on the analysis of various experimental results in the literature, Dinkelacker [16] claimed that the flame strain rate is the dominant factor in controlling the inner structure of premixed turbulent flames, and showed that no significant deviation of the flame front occurs from the thin laminar flamelet assumption for the conditions with turbulent Reynolds numbers smaller than 600. It was claimed that flame element interactions may lead to the formation of thick flame fronts [16].

Kortschik et al. [17] studied the influence of turbulence on temperature profile ahead of the preheat layers of low-swirl stabilized premixed turbulent flames in the thin reaction zones regime. Their results showed the existence of intense temperature fluctuations in front of the preheat layers of highly convoluted flame fronts, whereas the mean temperature profiles increased less severely with increasing non-dimensional turbulence intensity. They also showed that the probability density function of the temperature ahead of the preheat layers skewed towards higher temperatures by increasing the Karlovitz number from 0.98, that is, near the Klimov–Williams limit, to 12.5, that is, well within the thin reaction zones regime.

The brief review above shows that there is no consensus regarding the thickness of the turbulent flame front as the turbulence level is increased. In addition to the issue of whether the flame front thickness of highly convoluted flames is similar to the corresponding value of the stretched premixed laminar flame or to a thick flame front, there is still an existing question regarding the limit of the thin laminar flamelet regime beyond the Klimov–Williams criterion [10].

The thermal flame front thickness, specifically the measures that give characteristic dimensions of the preheat and reaction zones, was studied systematically in ultra-lean and lean premixed turbulent flames in the thin reaction zones regime. The influences of turbulence, equivalence ratio, and longitudinal integral length scale on the thermal flame front thickness were studied. The dominant mechanism for changing the inner structure of premixed turbulent flame fronts was inferred from these results. In addition, the influence of turbulence on the transportation of preheated turbulent structures in front of the preheat layers was examined by estimating the probability density function of the progress variable for different turbulence levels.

2. Experimental facility

2.1. Bunsen-type burner

The premixed turbulent flames were generated using an axisymmetric Bunsen-type burner with a nozzle inner diameter, D, of 22.2 mm as shown in Fig. 1. The burner is essentially the same as the one used in previous studies from this laboratory except that the present nozzle inner diameter is approximately twice as large as the previous one [18]. The air was filtered to eliminate any particles larger than 0.01 μm. The filtered air and methane grade 2.0 flow rates were controlled by calibrated mass flow meters. Each of the mass flow meter has an accuracy of ±0.80% on its reading, and ±0.20% on its full scale. Premixing of air and methane was achieved in a long tube containing 16 mm glass beads before entering into the burner assembly. The premixed reactants enter the burner assembly from the bottom part, Fig. 1(a), flow through the expansion section and the settling chambers with five mesh screens. The reactants are then accelerated into the contraction section with a contraction ratio of 84. The exit of the burner is located 200 mm downstream of the contraction section where the turbulent flame was anchored to the rim of the burner with an annular premixed ethylene/air pilot flame. For all experimental conditions, the turbulence was produced by positioning a perforated plate upstream of the burner exit. The perforated plate holes are arranged in a hexagonal array with a hole diameter of 1.8 mm. The mesh size and blockage ratio of the perforated plate are 2.6 mm and 60%, respectively.

2.2. Planar particle image velocimetry system

The instantaneous velocity vectors were measured using the planar particle image velocimetry technique. The light source

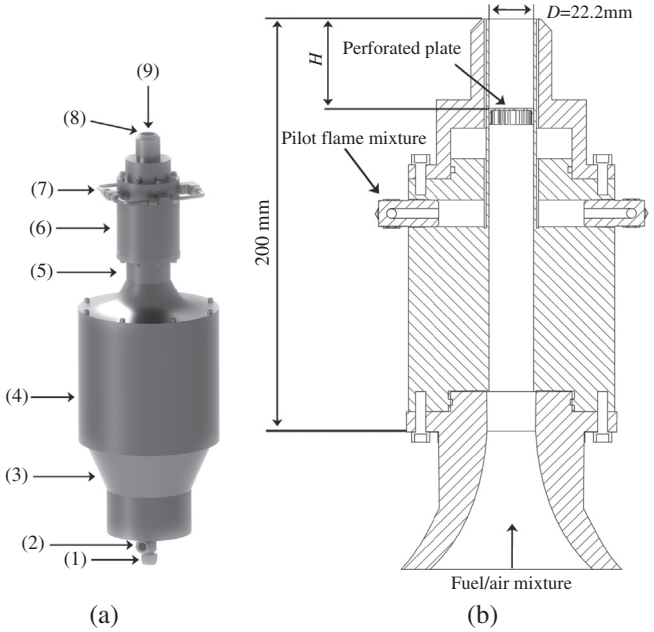

Fig. 1. (a) A 3D view of the Bunsen-type burner assembly: (1) reactants inlet; (2) seeding particles inlet; (3) expansion section; (4) settling chamber; (5) contraction section; (6) main body of the burner; (7) pilot flame mixture tubes; (8) pilot flame annular ring; (9) exit of the burner, and (b) cross-section of the main body.

was a double-pulsed Nd:YAG laser (Litron, Nano L 200-15) performing at an energy level and wavelength of 200 mJ/pulse and 532 nm, respectively. A LaVision light sheet optical assembly was utilized to form a laser sheet. It consisted of two spherical lenses, $f = +85$ and -75 mm, along with a cylindrical lens, $f = -20$ mm. The laser sheet had a full-width-at-half-maximum (FWHM) of approximately 300 μm at the burner centerline. The seeding particles in the flow field were generated by atomizing olive oil to sub-micron droplets using a nebulizer. A LaVision Imager pro X camera with a maximum resolution of $2{,}048 \times 2{,}048$ pixels^2 was used to record the experimental images. A Sigma macro lens was fitted to the camera with a focal length of 105 mm operating at $f/8$. A 532 nm bandpass filter was mounted on the lens to reduce the interference of undesired wavelengths from the surrounding environment on the camera's CCD. The camera was placed perpendicular to the laser sheet in order to maximize the light gathered from the seeding particles. In addition, a 355 nm bandpass filter was adjusted between the laser sheet and the burner exit to block the transmission of a section of the laser sheet that would be reflected from the edge of the burner to the camera's CCD.

The DaVis 7.2 software (FlowMaster, LaVision) was used to calculate the axial and radial velocity components. A three-dimensional calibration plate was utilized as a target for the calibration of the camera in order to map the location of the measurement plane on each pixel of the camera's CCD. For each experimental condition, five hundred image pairs were captured at a frequency of 6 Hz. A multi-pass vector evaluation technique was implemented to calculate the velocity components for each image pair with interrogation box sizes decreasing from 64×64 to 32×32 pixels^2 with a 50% overlap. This resulted in a resolution and vector spacing of approximately 900 and 450 μm, respectively. For each experimental condition, the time delay between laser pulses was adjusted in order to ensure that the displacement of seeding particles was less than a quarter of the final interrogation box size.

2.3. Planar Rayleigh scattering system

The temperature fields of premixed turbulent flames were measured using the planar Rayleigh scattering technique. A single-pulsed Nd:YAG laser (Spectra-Physics, Quanta-Ray, Lab-170-10) with a maximum energy of 220 mJ/pulse was used as a light source. A harmonic generator was fixed to produce a 355 nm wavelength at 5 Hz. A pair of dichroic mirrors was mounted after the harmonic generator to reflect the desired harmonic as an output wavelength, whereas undesirable wavelengths were transferred into a beam dump [19]. A Sodern-Cerco UV lens with a focal length of 94 mm operating at $f/4.1$ was fitted to an intensified CCD camera (NanoStar, LaVision) with a resolution of $1{,}280 \times 1{,}024$ pixels^2 to record the Rayleigh scattering images. The intensifier was active over a 10 μs period in order to reduce the influence of flame radiation on the Rayleigh scattering images. The gain for the ICCD was equal to 60. A 355 nm bandpass filter was attached to the lens to decrease the interference of other wavelengths from the surrounding environment on the camera's CCD. The magnification ratio for all experimental conditions is equal to 19.2 pixels/mm. It leads to have an approximately 19 pixels for a 1 mm flame front thickness. A UV-fused silica plano-concave lens, $f = -75$ mm, followed by a plano-convex lens, $f = +100$ mm, were used to focus the laser beam on the centerline of the burner. The focused beam was then converted into a laser sheet using a plano-concave cylindrical lens, $f = -25$ mm. This optical configuration resulted in a laser sheet of approximately 230 μm at full-width-at-half-maximum. It is estimated from the modulation transfer function of the current ICCD system using the methodology described by Wang and Clemens [20] that the in-plane spatial resolution is approximately 25 line-pairs/mm, and the out-of-plane spatial resolution is dictated by the laser sheet thickness.

3. Experimental conditions and data analysis

3.1. Experimental conditions

Three sets of experiments were completed in the current study. Conditions of these three sets consisting of 14 flames are tabulated in Table 1. In the first set of experiments, the equivalence ratio was fixed at $\phi = 0.6$, whereas the bulk flow velocity range was from 17 to 46 m/s. As a result, the geometric Reynolds number based on the bulk flow velocity and the burner diameter covered a range from

Table 1
Summary of experimental conditions.

Set of experiments	Flame	ϕ[a]	U_B (m/s)[b]	S_L^0 (m/s)[c]	u'/S_L^0[d]	Λ_L/δ_f[e]	Re_D[f]	Re_{Λ_L}[g]	Ka[h]
I	A	0.6	17	0.118	5.5	12.7	24,036	96	4.2
	B	0.6	25	0.118	8.0	13.5	35,347	150	7.3
	C	0.6	30	0.118	9.6	12.6	42,417	168	9.9
	D	0.6	36	0.118	12.1	13.5	50,900	224	13.4
	E	0.6	39	0.118	13.3	13.7	55,142	251	15.3
	F	0.6	43	0.118	14.2	13.0	60,797	254	17.4
	G	0.6	46	0.118	16.5	14.5	65,039	330	20.7
II	H	0.7	36	0.198	7.2	23.1	50,900	231	4.8
	I	0.8	36	0.279	5.1	32.3	50,900	227	2.4
	J	0.9	36	0.345	4.2	39.5	50,900	228	1.6
	K	1.0	36	0.386	3.7	46.1	50,900	236	1.2
III	L	0.7	16	0.198	4.0	17.8	22,622	98	3.0
	M	0.7	24	0.198	4.0	25.3	33,933	141	2.6
	N	0.7	28	0.198	3.9	31.5	39,589	171	2.3

[a] ϕ is the equivalence ratio.
[b] U_B is the bulk flow velocity.
[c] S_L^0 is the unstrained premixed laminar burning velocity calculated by the Cantera package [21] with the GRI-Mech 3.0 mechanism [22].
[d] u'/S_L^0 is the ratio of the total turbulence intensity to the unstrained premixed laminar burning velocity.
[e] Λ_L/δ_f is the ratio of the longitudinal integral length scale to the Zel'dovich thickness. The Zel'dovich thickness, δ_f, was calculated by determining the ratio of the reactant mass diffusivity to the unstrained premixed laminar burning velocity [23].
[f] Re_D is the geometric Reynolds number based on the bulk flow velocity, U_B, and the burner diameter, D.
[g] Re_{Λ_L} is the turbulent Reynolds number based on the total turbulence intensity, u', and the longitudinal integral length scale, Λ_L.
[h] Ka is the Karlovitz number, and was evaluated from $Ka = (\delta_f/\eta)^2$, where the Kolmogorov length scale, η, was calculated from $\eta = \Lambda_L Re_{\Lambda_L}^{-3/4}$.

Please cite this article in press as: P. Tamadonfar, Ö.L. Gülder, Combust. Flame (2014), http://dx.doi.org/10.1016/j.combustflame.2014.07.001

24,000 to 65,000. The perforated plate was mounted at two burner diameters upstream of the burner exit for this set (as well as the second set). In the second set of experiments, the equivalence ratio was changed from 0.6 to 1.0 at a constant bulk flow velocity of 36 m/s giving a geometric Reynolds number of 50,900. For the second set of conditions (including Flame D from the first set), the turbulent Reynolds number was almost constant (224–236). In the third set of experiments, the equivalence ratio was constant at $\phi = 0.7$. In order to change the longitudinal integral length scale, the location of the perforated plate was varied from one burner diameter to seven burner diameters upstream of the burner exit, from Flame L to Flame N, whereas the bulk flow velocity was changed from 16 to 28 m/s in order to keep the total turbulence intensity constant.

The total turbulence intensity and turbulent integral length scale are relatively important parameters in comparison with other turbulence properties in the flame/flow interactions. These properties are controlled by the geometry and upstream position of the turbulence generator from the burner exit [24,25]. The $\langle u^2\rangle^{1/2}$, $\langle v^2\rangle^{1/2}$, and $\langle w^2\rangle^{1/2}$ are the root-mean-square (r.m.s) of velocity fluctuations in the axial, radial, and azimuthal directions, respectively. Due to the axisymmetric nature of the flow, the r.m.s of radial and azimuthal velocity fluctuations were assumed to be equal. Therefore, the total turbulence intensity, u', was calculated using the following relation:

$$u' = \left(\frac{\langle u^2\rangle + \langle v^2\rangle + \langle w^2\rangle}{3}\right)^{1/2} = \left(\frac{\langle u^2\rangle + 2\langle v^2\rangle}{3}\right)^{1/2}. \quad (1)$$

As a representative plot, the r.m.s of axial, radial, and total velocity fluctuations normalized by the bulk flow velocity at $h/D = 0.50$ with respect to the normalized radial distance, r/D, are shown in Fig. 2(a)–(c), respectively, where h is the axial distance from the burner exit, and r is the radial distance from the centerline of the burner. These profiles were obtained by conducting the first set of experiments under non-reacting conditions. These profiles were almost uniform for $r/D < 0.3$, and they increased significantly near the edge of the burner, that is, $r/D \simeq 0.5$. Experimental measurements of Chen and Bilger [24] displayed a similar trend.

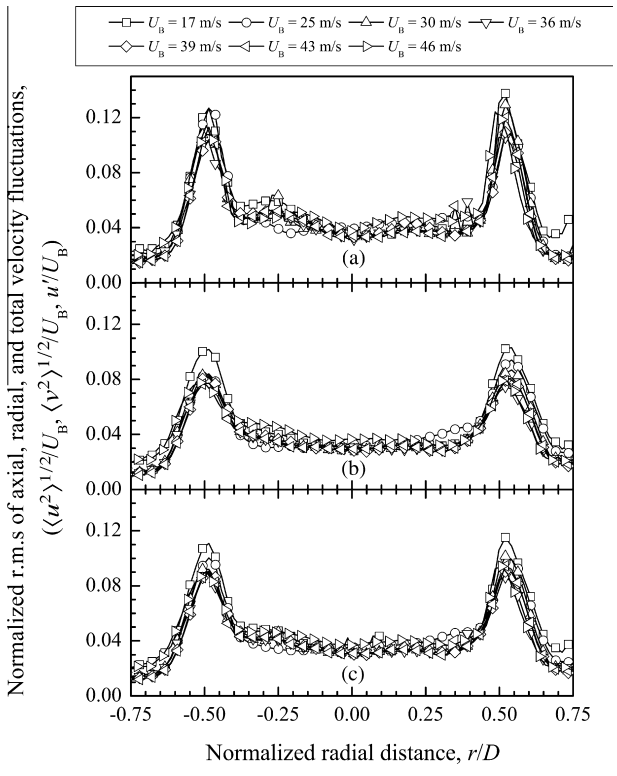

Fig. 2. Normalized r.m.s of (a) axial, (b) radial, and (c) total velocity fluctuations at different bulk flow velocities with respect to the normalized radial distance at $h/D = 0.50$. These profiles were generated by conducting the first set of experiments under non-reacting conditions.

For each experimental condition, the total turbulence intensity was averaged in a region between $-0.25 < r/D < 0.25$ and $0.1 < h/D < 0.5$. The total turbulence intensities for all three sets of experiments are shown in Fig. 3(a)–(c). Error bars represent uncertainties in the total turbulence intensity with a 95% confidence interval. In the first set of experiments, the total turbulence intensity varied linearly with the geometric Reynolds number under the reacting and non-reacting conditions, Fig. 3(a). The magnitudes of the total turbulence intensity at a constant geometric Reynolds number were almost constant under the reacting and non-reacting conditions since the averaging area was located in the unburned region. In the second set, the total turbulence intensity seemed to be insensitive to the equivalence ratio at a constant bulk flow velocity of 36 m/s, Fig. 3(b). In the third set, the total turbulence intensity normalized by the bulk flow velocity, u'/U_B, decreased from 5% to 2.8% by changing the location of the turbulence generator from one diameter to seven diameters upstream of the burner exit, Fig. 3(c). Therefore, the bulk flow velocity was increased from 16 to 28 m/s in order to keep the total turbulence intensity constant, Fig. 3(c).

The longitudinal and transverse integral length scales (Λ_L and Λ_T) were estimated from the longitudinal and transverse velocity correlation coefficients ($f(\triangle x)$ and $g(\triangle x)$), respectively [26]. These correlations were estimated using the following formulas:

$$f(\triangle x) = \frac{\langle u(h)u(h+\triangle x)\rangle}{\langle u(h)^2\rangle}, \quad (2a)$$

$$g(\triangle x) = \frac{\langle v(h)v(h+\triangle x)\rangle}{\langle v(h)^2\rangle}, \quad (2b)$$

where u and v are the velocity fluctuations in the axial and radial directions, respectively, and $\triangle x$ is the velocity vector spacing in the axial direction. The profiles of the longitudinal and transverse velocity correlation coefficients for a typical experimental condition, Flame D, are shown in Fig. 4.

The longitudinal and transverse integral length scales were then measured using the following expressions:

$$\Lambda_L = \int_0^{\triangle x_L^*} f(\triangle x)\mathrm{d}\triangle x, \quad (3a)$$

$$\Lambda_T = \int_0^{\triangle x_T^*} g(\triangle x)\mathrm{d}\triangle x, \quad (3b)$$

where $\triangle x_L^*$ and $\triangle x_T^*$ are the first zero crossing locations of $f(\triangle x)$ and $g(\triangle x)$, respectively. For each experimental condition, the longitudinal and transverse integral length scales were averaged in a region between $-0.25 < r/D < 0.25$ and $0.1 < h/D < 0.5$. These length scales for all three sets of experiments are shown in Fig. 5(a)–(c). Error bars correspond to twice the standard deviation of integral length scales in the averaging area of each experimental condition. In the first set of experiments, the longitudinal and transverse integral length scales seemed to be insensitive to the geometric Reynolds number under the reacting and non-reacting conditions, Fig. 5(a). In the second set, these scales were found to be constant with increasing equivalence ratios from 0.6 to 1.0, Fig. 5(b). In the third set, the longitudinal integral length scale increased by approximately 75% by changing the location of the turbulence generator from one burner diameter to seven burner diameters upstream of the burner exit, Fig. 5(c). The ratios of the transverse to the longitudinal integral length scales were close to one half

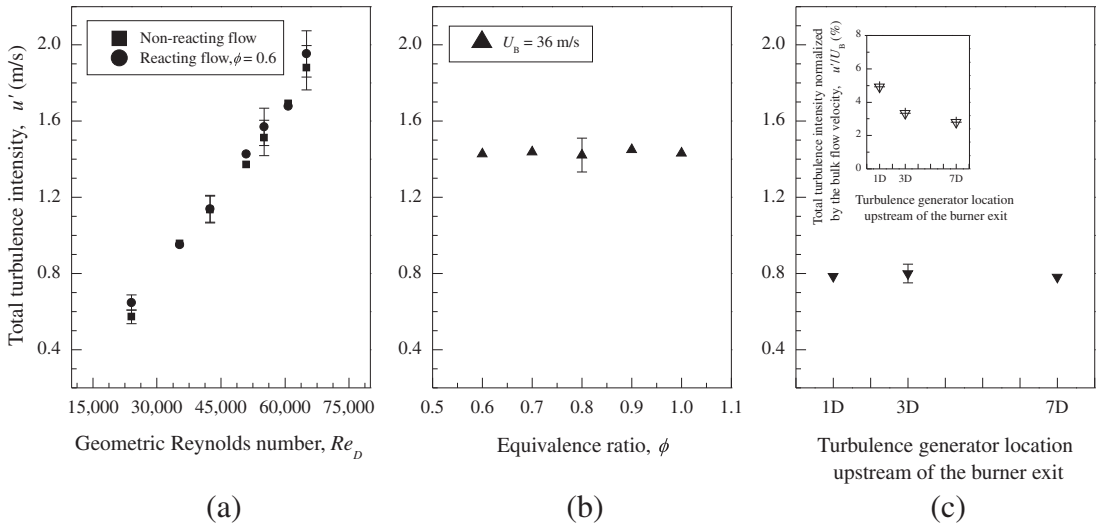

Fig. 3. Total turbulence intensity as a function of (a) the geometric Reynolds number, (b) the equivalence ratio, and (c) the turbulence generator location upstream of the burner exit.

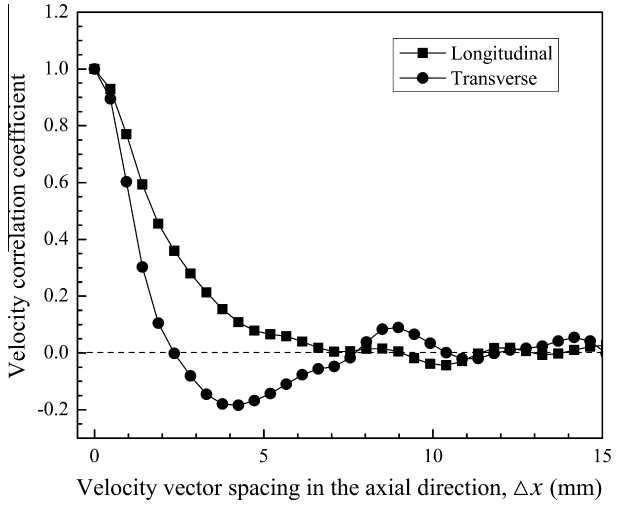

Fig. 4. Longitudinal and transverse velocity correlation coefficients as a function of the velocity vector spacing in the axial direction on the centerline of the burner at $h/D = 0.50$ for Flame D.

for all experimental conditions, and they were consistent with the isotropic turbulence assumption proposed in [26].

The experimental conditions were plotted on a Borghi–Peters regime diagram for premixed turbulent combustion [3,27] as shown in Fig. 6. It is observed that all experimental conditions are mainly located in the thin reaction zones regime since all Karlovitz numbers are greater than unity.

3.2. Two-dimensional temperature measurement

The DaVis 7.0 software (Rayleigh Thermometry, LaVision) was used to record the Rayleigh scattering images. Five hundred images were recorded for each experimental condition. The imaging zone was restricted between two to four diameters downstream of the burner exit. A 3×3 pixels^2 non-linear sliding average filter was applied on each raw image to reduce the existing noise. In a typical filtered Rayleigh scattering image, the intensity was about 270 counts in the unburned region, and it reduced to 140 counts in the burned region. The signal-to-noise ratio (SNR) was evaluated by defining a box of 10×10 pixels^2 and determining the ratio of the mean to the standard deviation of the intensity counts in the

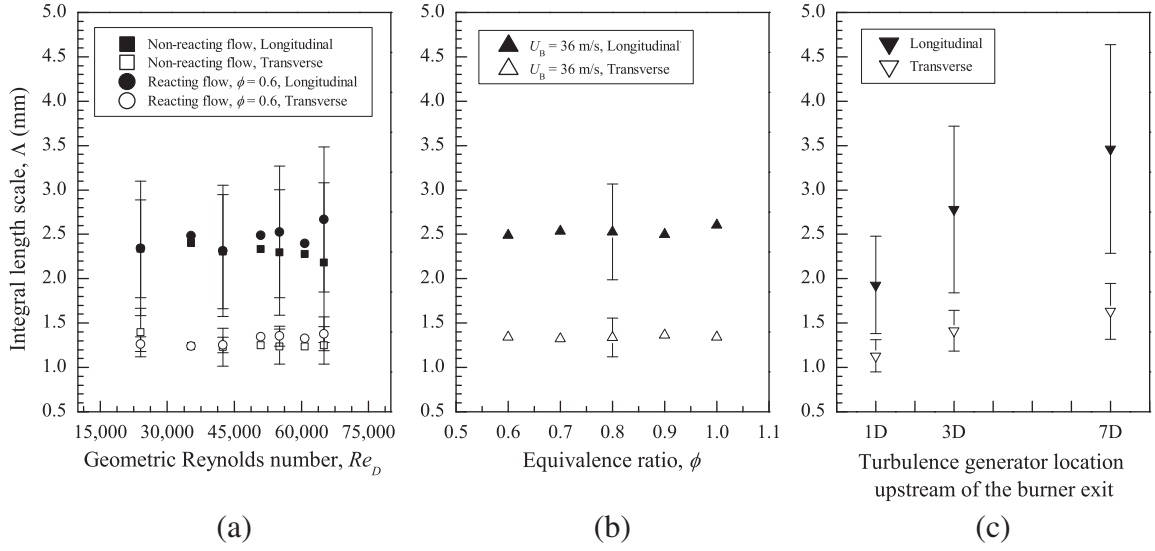

Fig. 5. Integral length scale as a function of (a) the geometric Reynolds number, (b) the equivalence ratio, and (c) the turbulence generator location upstream of the burner exit.

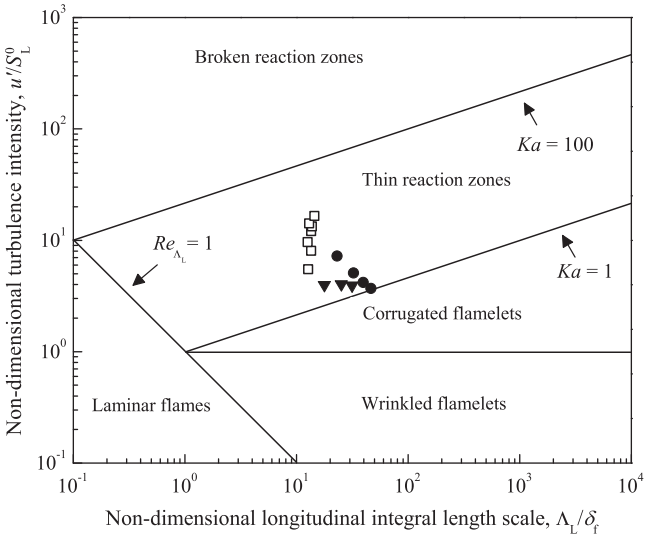

Fig. 6. Experimental conditions on a Borghi–Peters regime diagram for premixed turbulent combustion [27,3]. Open squares – Flames A–G; full circles – Flames H–K; full triangles – Flames L–N.

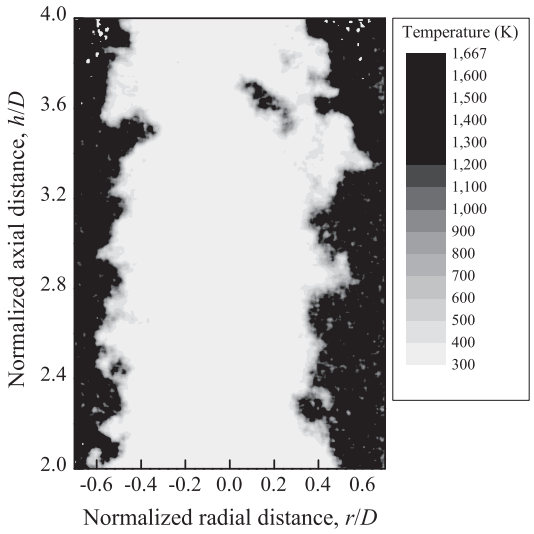

Fig. 7. Instantaneous two-dimensional temperature field for Flame A.

unburned and burned regions. Therefore, the signal-to-noise ratio for a typical flame condition was approximately 13.5 and 5.5 in the unburned and burned regions, respectively. The flame temperature, $T_f(r,h)$, was calculated using the following formula [12]:

$$T_f(r,h) = \frac{\sigma_m}{\sigma_a} T_a \frac{I_a - I_b}{I_R - I_b} = kT_a I, \tag{4}$$

These σ_m and σ_a are the fuel–air mixture and pure-air Rayleigh scattering cross sections, respectively. These parameters were evaluated from $\sigma_m = (\sum_i \sigma_i \chi_i)_m$ and $\sigma_a = (\sum_i \sigma_i \chi_i)_a$. The Rayleigh scattering cross section, σ_i, of the ith species was obtained from Sutton and Driscoll [28]. The dependency of the temperature on the Rayleigh scattering cross section was not included in Eq. (4) due to its insignificant variation at 355 nm [28]. The mole fraction of each species, χ_i, was evaluated by solving an adiabatic unstrained premixed laminar flame using the Cantera package [21]. T_a is the air temperature. I_R, I_a, and I_b are the intensity of the flame, reference, and background images, respectively. The reference image was recorded under the non-reacting condition, where the co-flow was utilized to eliminate dust particles from the measurement area. Knaus et al. [29] suggested a method for estimating the background intensity. Based upon this method, Eq. (4) was solved in the burned region by fixing $T_f = T_{ad}$, where T_{ad} is the adiabatic flame temperature. The averaged background intensity was approximately 115 counts for all experimental conditions, and it was almost 30% higher than the dark image intensity counts. The intensity ratio, I, showed a bimodal distribution for each image. The peaks of the intensity ratio were associated with the unburned and burned temperatures [18]. A 4th order polynomial was then used to establish a correlation between the intensity ratio, I, and the ratio of the fuel–air mixture to the pure-air Rayleigh scattering cross sections, k, within the range of these peaks for each image. Therefore, the R.H.S of Eq. (4) is dependent on a single parameter of I only at a fixed T_a. An instantaneous temperature field for a typical flame condition, Flame A, is shown in Fig. 7.

3.3. Two-dimensional turbulent thermal flame front thickness

The temperature gradient of the normal temperature profile across the flame front can be used directly to estimate the instantaneous thermal flame front thickness of the premixed turbulent flame. However, creating normal profiles on all the flame front positions is fairly complex for highly wrinkled premixed flames [30]. This issue was solved by conditioning the two-dimensional temperature gradient field, $\nabla T_f(r,h)$, at a specific progress variable, c, for each temperature field. The two-dimensional turbulent thermal flame front thickness, $\delta_{T,c}$, was then evaluated using the following relation:

$$\delta_{T,c} = \frac{T_b - T_u}{\nabla T_f(r,h)|_c}, \tag{5}$$

where T_b and T_u are the burned and unburned temperatures, respectively. The two-dimensional temperature gradient, $\nabla T_f(r,h)$, was calculated using the following expression:

$$\nabla T_f(r,h) = \left(\left(\frac{T_f(r+\Delta r,h) - T_f(r-\Delta r,h)}{2\Delta r} \right)^2 + \left(\frac{T_f(r,h+\Delta h) - T_f(r,h-\Delta h)}{2\Delta h} \right)^2 \right)^{1/2}, \tag{6}$$

where Δr and Δh are the pixel resolutions in the radial and axial directions, respectively. An instantaneous two-dimensional temperature gradient field for a representative flame condition, Flame G, and the locations of the flame fronts at two distinct progress variables, that is, $c = 0.3$ and 0.5, are shown in Fig. 8(a). The uncertainties associated with the evaluation of these progress variable contours are about 10%. The main source of the uncertainty in the evaluation of progress variable contour originates from the existing noise in the Rayleigh scattering measurements. It is assumed that the distribution of noise in this system is Gaussian. This uncertainty increases with increasing progress variable due to the decrease in the signal-to-noise ratio. Therefore, no conclusion can be extracted from the results at large progress variables. This level of uncertainty in the progress variable is comparable to previous measurements in the literature, see, e.g., [12,17,31]. The probability density functions of the temperature gradient for all recorded images of Flame G conditioned at these progress variables displayed nearly Gaussian distributions, Fig. 8(b). Similar observations were previously reported in [12,32]. The uncertainty associated with the estimation of temperature gradient is approximately two times the uncertainty in the temperature measurement. It should be stated that the temperature gradient values in the tails of the distribution are heavily influenced by the existence of noise due to the Gaussian distribution of noise, whereas the influence of noise on the temperature gradient is minimal near the mean temperature

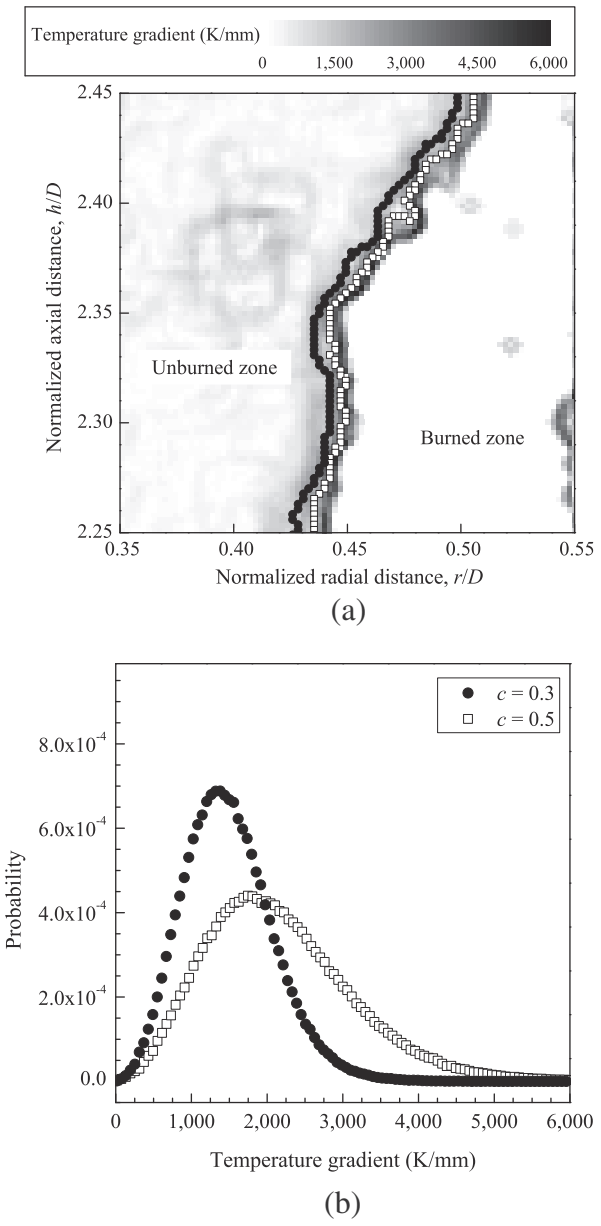

Fig. 8. (a) Instantaneous two-dimensional temperature gradient field along with the flame fronts at two different progress variables for Flame G. Full circle – $c = 0.3$; open square – $c = 0.5$, and (b) probability density functions of two-dimensional temperature gradient conditioned at $c = 0.3$ and 0.5 for all captured images of Flame G.

gradient. It is worth mentioning that the occurrence of a negative temperature gradient across the flame front of the premixed turbulent flame was not considered in Eq. (6). This issue will be discussed in detail in Section 3.6.

The preheat zone thickness was characterized by conditioning the temperature gradient at $c = 0.3$ [12], and the characteristic behavior of the reaction zone thickness was measured by conditioning the temperature gradient at $c = 0.5$ [31].

3.4. Effect of flame stretch on the thermal flame front thickness

The flame stretch is the rate of change of flame surface area [33]. It consists of two discrete components, that is, the flame strain rate (α), and the flame front curvature (κ) [34]. In this study, the evaluation of flame strain rate and its effect on the turbulent thermal flame front thickness were not quantitatively possible since simultaneous measurements of instantaneous velocity fields and flame front positions would be required. Therefore, in order to isolate the effect of flame strain rate on the turbulent thermal flame front thickness without quantifying the flame strain rate, the flame front thicknesses were acquired at zero-curvature flame fronts under different turbulence levels. Furthermore, these results were compared with flame front thicknesses of strained premixed laminar flames. This comparison may explain whether or not the behavior of flame front thicknesses of highly turbulent flames were similar to the corresponding values of strained premixed laminar flames. For this reason, the numerical simulations were performed on premixed laminar counterflow methane/air flames using the Cantera package [21] under different strain rates, and the thermal flame front thicknesses were evaluated from the acquired temperature profiles using Eq. (5). These numerical results indicate the influence of flame strain rate in the absence of a flame front curvature on the strained premixed laminar flame front thickness.

The two-dimensional flame front curvature was evaluated to examine its influence on the thermal flame front thickness using the following expression [35]:

$$\kappa = \frac{\frac{dr}{ds}\frac{d^2h}{ds^2} - \frac{dh}{ds}\frac{d^2r}{ds^2}}{\left[\left(\frac{dr}{ds}\right)^2 + \left(\frac{dh}{ds}\right)^2\right]^{3/2}}, \tag{7}$$

where r and h are the coordinates of the flame front, and s is the parametrized arc length. The flame front and its derivatives were filtered using a zero-phase digital filter which is a built-in script in MATLAB. The filter length was selected to be five points to preserve the structure of the flame front thickness smaller than the laminar condition. A representative instantaneous flame front, Flame G, filtered with a zero-phase digital filter is shown in Fig. 9. The flame front curvature is positive when it was convex towards the reactants. The resolvable flame front curvature is $\pm 4.3\ \mathrm{mm}^{-1}$ due to the restriction on the laser sheet thickness. The uncertainty associated with measurement of the flame front curvature, with a 95% confidence interval, is estimated to be approximately 5%.

3.5. Flame front widening

The widening of the premixed turbulent flame front was investigated using a method proposed by Shepherd et al. [30]. The area

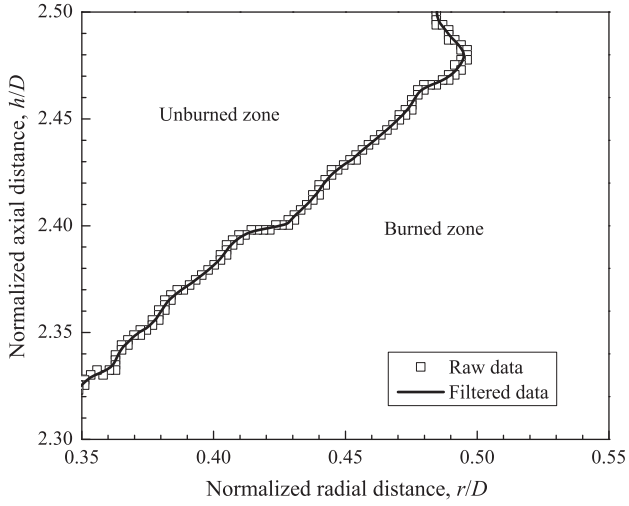

Fig. 9. Instantaneous flame front selected at $c = 0.5$ for Flame G. Open squares – raw data; solid line – filtered data.

between the progress variable contours, $c_{p,q}$, of the premixed turbulent flame becomes wider in comparison with the unstrained premixed laminar flame when the influence that turbulent eddies have on changing the internal structure of the flame front is significant [30]. This area was estimated by multiplying the area of one pixel with the number of pixels between the progress variable contours of p and q for each instantaneous progress variable image. The mean relative effect of turbulent widening was then estimated by comparing the ratios of these areas acquired from the turbulent flame to the corresponding values obtained from the unstrained premixed laminar flame. Shepherd et al. [30] argued that these areas include other flame front broadening mechanisms such as the out-of-plane flame tilting and flame front curvature. Therefore, this method provides a tool for investigating the effect of turbulent structures on mean flame front widening.

3.6. Temperature profile normal to the flame front

It was mentioned in Section 3.3 that the negative temperature gradient across the flame front of the premixed turbulent flame cannot be estimated using Eq. (6). Three thousand normal temperature profiles across the flame fronts of premixed turbulent flames were constructed in order to estimate the number of temperature profiles with negative temperature gradients. Two temperature profile samples normal to the flame front for a representative flame condition, Flame D, are shown in Fig. 10. The origin of these temperature profiles, $G = 0$, was fixed at $T = 710$ K ($c = 0.3$). The temperature profile of sample 1 is similar to the unstrained premixed laminar flame, whereas significant temperature rise is observed in front of the preheat zone as well as the negative temperature gradient at $G = 0$ for sample 2. It is believed that the temperature rise ahead of the preheat zone is due to the transportation of the preheated gas from the reaction zone to this region [17]. The existence of a negative temperature gradient at $G = 0$ may be due to the interaction of flame front layers with one another. This results in the deviation of the temperature profile from the thin laminar flamelet assumption. The number of temperature profiles with negative temperature gradients at $G = 0$ was then estimated to be approximately 50 profiles (less than 1.7%) for all three select conditions. These insignificant numbers were assumed to be valid for all experimental conditions studied in this work. Therefore, using Eq. (5) for calculating the turbulent thermal flame front thickness seemed to be appropriate considering the insignificant influence that the negative temperature gradient might have on the results. In addition, the effect of turbulence on the mean progress variable profile as well as the probability density function of the progress variable ahead of the preheat layers will be discussed in Section 4 for these select conditions.

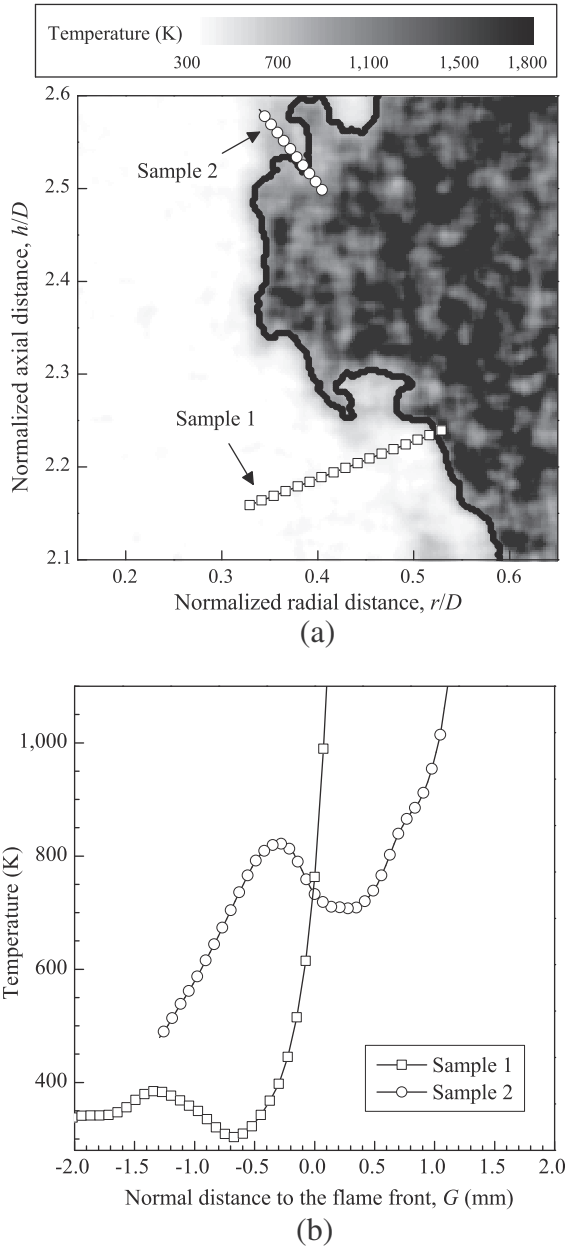

Fig. 10. (a) Instantaneous flame front selected at $c = 0.3$ superimposed on the temperature field along with two temperature profile samples normal to the flame front, and (b) two temperature profile samples normal to the flame front for Flame D.

4. Results and discussion

The probability density functions of two-dimensional preheat zone and reaction zone thicknesses for Flame D normalized by the corresponding values of the unstrained premixed laminar flame are shown in Fig. 11. The shapes of both distributions are similar to a log-normal distribution, and similar observations were previously reported in [18,31,36]. For the current condition, the occurrences of the preheat zone and reaction zone thicknesses smaller than the similar values of the unstrained premixed laminar flame are about 75%.

Dinkelacker et al. [31] claimed that the peak value of the two-dimensional thermal flame front thickness distribution is a rough approximation of the three-dimensional value. Therefore, the representative value of the thermal flame front thickness, in this study, was evaluated by finding the peak value of the two-dimensional thermal flame front thickness distribution for each flame condition. The temperature gradient used for estimating the representative flame front thickness is located near the mean temperature gradient where the effect of noise on the temperature gradient is minimal, whereas near zero flame front thicknesses and extremely thick flame fronts correspond to the regions where the uncertainties in the temperature gradients are high due to the existence of noise. It should be mentioned that the magnification ratio of the current experiments is sufficient to resolve the thermal flame front thickness. The effect of the magnification ratio on the preheat zone and reaction zone thicknesses is quantified in Appendix A. The normalized preheat zone and reaction zone thicknesses as a function of the non-dimensional turbulence intensity, u'/S_L^0, for the first set of experiments are shown in Fig. 12. The preheat zone and reaction zone thicknesses are smaller than the

corresponding values of the unstrained premixed laminar flame. Moreover, increasing the non-dimensional turbulence intensity from 5.5 to 16.5 reduces the normalized preheat zone and reaction zone thicknesses by approximately 23% and 26%, respectively. This decreasing trend of the flame front thickness with turbulence was previously reported for swirl-stabilized methane/air flames for the non-dimensional turbulence intensity changing from 3.5 to 18.7 under a constant equivalence ratio of 0.7 [14].

The existence of thin preheat zone thickness for Flames A–G opposes the well-known hypothesis proposed for the thin reaction zones regime [3], where the penetration of small turbulent structures is assumed to broaden the preheat zone and enhance the turbulent mixing process. The possible reason behind the formation of thin preheat zones may be due to the destruction of small turbulent eddies in the presence of high viscosity gradients across the turbulent flame fronts [12,14].

To understand the mechanism behind the thinning of the flame front with increasing non-dimensional turbulence intensity (see Fig. 12), the effect of flame strain rate on the preheat zone and reaction zone thicknesses of the strained premixed laminar flame was studied numerically, and its response was compared qualitatively with the first set of experimental data. Numerical simulations were performed by solving planar, counterflow premixed methane/air flames using the Cantera package [21]. The temperature and its gradient profiles were calculated across the flame front for different strain rates as well as the unstrained condition under a constant equivalence ratio of 0.6, Fig. 13. The temperature gradient increases considerably by increasing the imposed strain rate on the flame front, resulting in a significant decrease in the flame front thickness. The reduction of flame front thickness with the strain rate for lean premixed laminar flames with a Lewis number of unity was previously observed by Darabiha et al. [37]. Furthermore, Sung et al. [38] studied the structure of nonequidiffusive laminar flames (methane/air, hydrogen/air, and propane/air) in counterflow, and showed that the flame front thickness decreases by exerting a positive strain rate on lean methane/air and hydrogen/air flames, whereas it increases for lean propane/air flames. In addition, Najm and Wyckoff [39] studied the interaction of a two-dimensional counter-rotating vortex pair on a premixed stoichiometric methane/air flame, and reported that the flame front thickness is increased (decreased) by decreasing (increasing) the flame strain rate.

The preheat zone and reaction zone thicknesses were acquired at zero-curvature flame fronts for the first set of experiments. These results are compared to corresponding values of strained premixed laminar flames under different Karlovitz numbers, Fig. 14. The ratios of the preheat zone and reaction zone thicknesses of turbulent and strained premixed laminar flames to the corresponding values of the unstrained premixed laminar flame were less than unity for these conditions. The experimental data and the numerical results show a similar behavior, and they decay exponentially with the Karlovitz number. Based on this observation, it can be stated that increasing the total strain rate with increasing turbulence results in a considerable decrease in the preheat zone and reaction zone thicknesses.

The influence of normalized flame front curvature on the normalized preheat zone and reaction zone thicknesses for the first set of experiments is shown in Fig. 15(a) and (b), respectively. The preheat zone and reaction zone thicknesses are found to become larger with the flame front curvature, and the minimum values occur at zero-curvature flame fronts. This increase may be due to the existence of local compressive strain rates at large flame front curvatures [39]. The preheat zone and reaction zone thicknesses are found to become smaller by increasing the non-dimensional turbulence intensity at a fixed flame front curvature. Furthermore, the rate of flame front thickening from zero-curvature flame fronts up to its maximum value is approximately 37% for the preheat zone and 32% for the reaction zone. The amount of thickening is equally distributed between the positive and negative curvatures, and similar observations were previously reported in [18,36]. On the other hand, some studies showed that the existence of local compressive strain rates create thicker flame fronts at high positive curvatures in comparison with the flame fronts with negative curvatures, see, e.g., [8,39]. In addition, Sankaran et al. [8] studied the influence of several terms (dilatation, tangential strain rate, normal gradient of kinematic restoration, and normal gradient of curvature component of propagation) that affect the flame front thickness, and showed that the dominant source of flame front thickening at large flame front curvatures is the normal gradient of curvature component of propagation.

The effect of the equivalence ratio on the preheat zone and reaction zone thicknesses was investigated at a constant bulk flow velocity of 36 m/s for the second set of experiments (including Flame D). The normalized preheat zone and reaction zone thicknesses increase with increasing equivalence ratios from 0.6 to 1.0, Fig. 16. Similar trends were previously reported for the bluff-body stabilized flames [13] and swirl-stabilized flames [14]. Most importantly, these normalized thicknesses are less than unity for

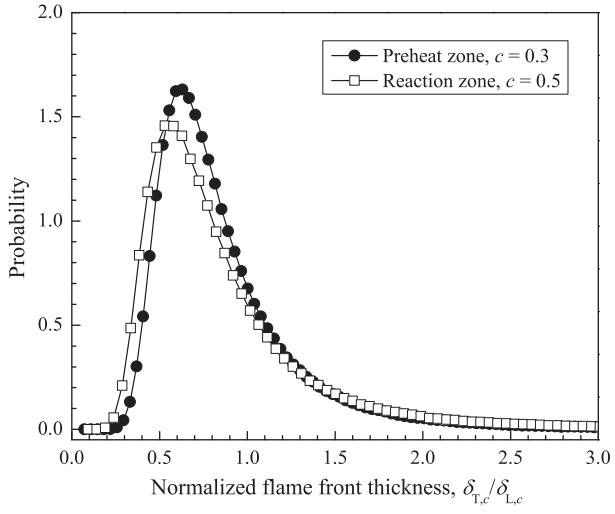

Fig. 11. Probability density functions of the normalized preheat zone and reaction zone thicknesses for Flame D.

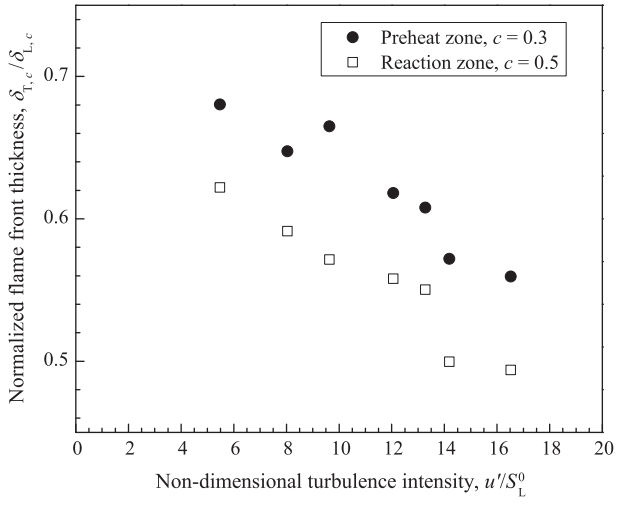

Fig. 12. Normalized preheat zone and reaction zone thicknesses as a function of the non-dimensional turbulence intensity for the first set of experiments.

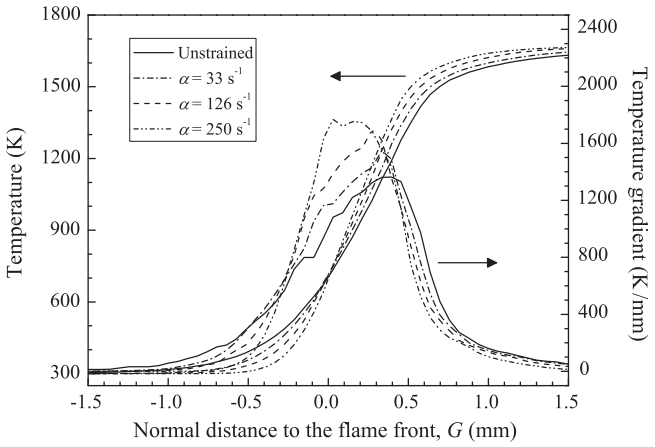

Fig. 13. Temperature and its gradient profiles across the flame front of the strained premixed laminar flame for different strain rates at an equivalence ratio of 0.6. The solid line corresponds to the unstrained condition.

equivalence ratios of 0.6 and 0.7. On the other hand, the creation of thick flame fronts for equivalence ratios varying from 0.8 to 1.0 indicates that the internal structure of the flame fronts deviates from the thin laminar flamelet assumption.

The mean relative effect of turbulent widening for the three different conditions, $c_{3.5}/c_{2.6}$, $c_{3.5}/c_{2.8}$, and $c_{4.6}/c_{2.8}$, was calculated for the second set of experiments (including Flame D from the first set) and is shown Fig. 17. Results indicate that there is not any systematic trend with the equivalence ratio, and the mean widening for progress variable contours of premixed turbulent flames in comparison with corresponding values of unstrained premixed laminar flames seems to be negligible. This observation implies that the small turbulent eddies may not be the reason behind the formation of thick flame fronts shown in Fig. 16.

To explain the probable reason behind the creation of thick flame fronts, the preheat zone and reaction zone thicknesses of a strained premixed laminar flame were computed at $\alpha = 2,000\ s^{-1}$ for different equivalence ratios as shown in Fig. 16. Numerical results reveal that the normalized preheat zone and reaction zone thicknesses decreased with the flame strain rate for equivalence ratios varying from 0.6 to 1.0. In addition, it was shown that the flame front thickness is overestimated when computed using the 2D Rayleigh scattering images [14]. Based on these observations, it can be stated that the formation of thick flame fronts for equivalence ratios varying from 0.8 to 1.0 may be attributed to the 2D image processing, whereas the effect of flame strain rate on thinning the flame fronts seems to be of minor significance. On the other hand, the presence of thin flame fronts for equivalence ratios of 0.6 and 0.7 may be due to a dominant influence of flame strain rate on thinning the flame fronts. This effectively compensates for the flame front thickness overestimation that may be imparted by the 2D image processing.

The normalized preheat zone and reaction zone thicknesses seem to be insensitive to the non-dimensional longitudinal integral length scale for the third set of experiments as shown in Fig. 18. This trend may be attributed to the insignificant differences in Karlovitz numbers. Furthermore, these normalized thicknesses are smaller than unity, indicating that the thin laminar flamelet assumption is valid for the conditions of the third set of experiments (Table 1).

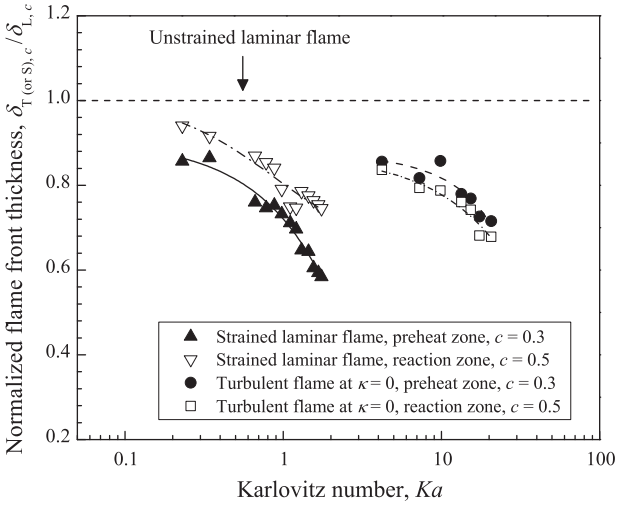

Fig. 14. Normalized preheat zone and reaction zone thicknesses as a function of the Karlovitz number. The turbulent conditions are for the first set of experiments. The lines are least squares fits to the data. Solid line – $c = 0.3$, strained laminar flame; Dash dot line – $c = 0.5$, strained laminar flame; Dash line – $c = 0.3$, turbulent flame; short dash dot – $c = 0.5$, turbulent flame.

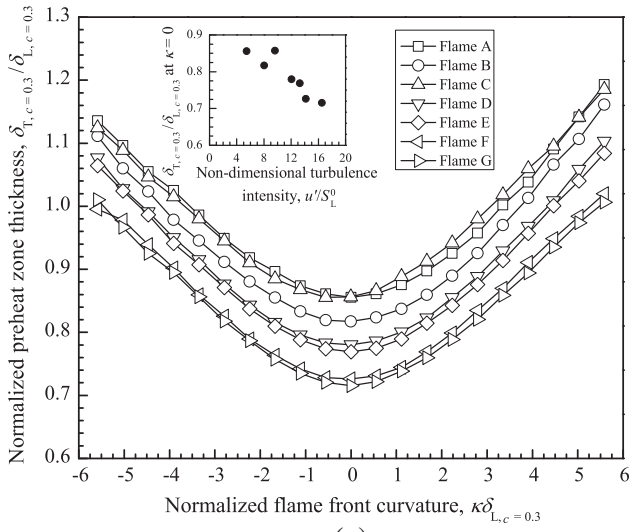

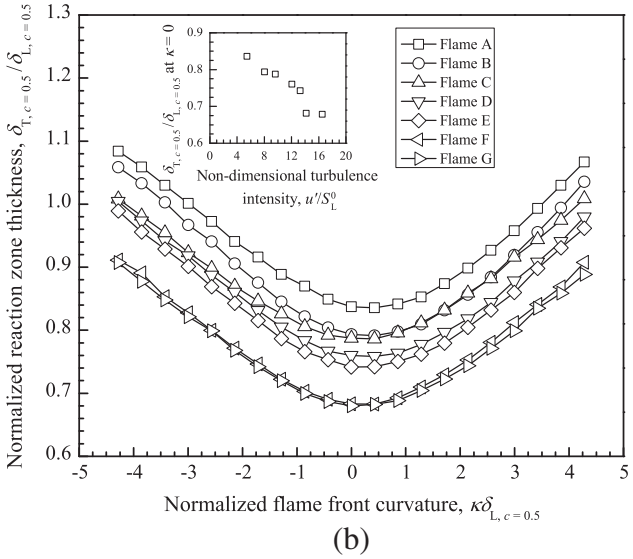

Fig. 15. (a) Normalized preheat zone thickness, and (b) normalized reaction zone thickness with respect to the normalized flame front curvature for the first set of experiments.

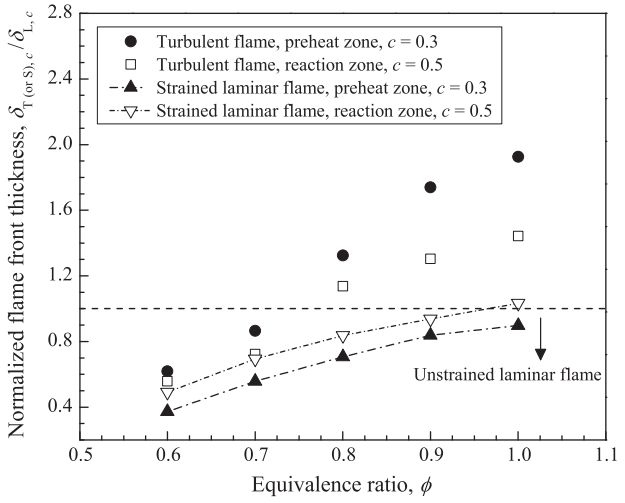

Fig. 16. Normalized preheat zone and reaction zone thicknesses as a function of the equivalence ratio for the second set of experiments (including Flame D) as well as the strained premixed laminar flame calculated at $\alpha = 2,000\ s^{-1}$.

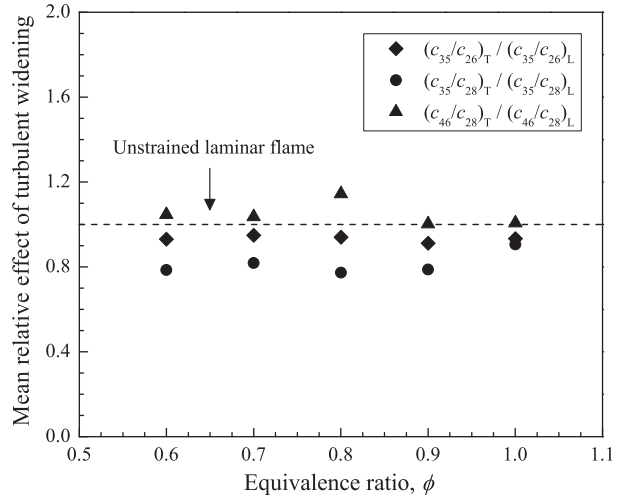

Fig. 17. Mean relative effect of turbulent widening as a function of the equivalence ratio for the second set of experiments (including Flame D).

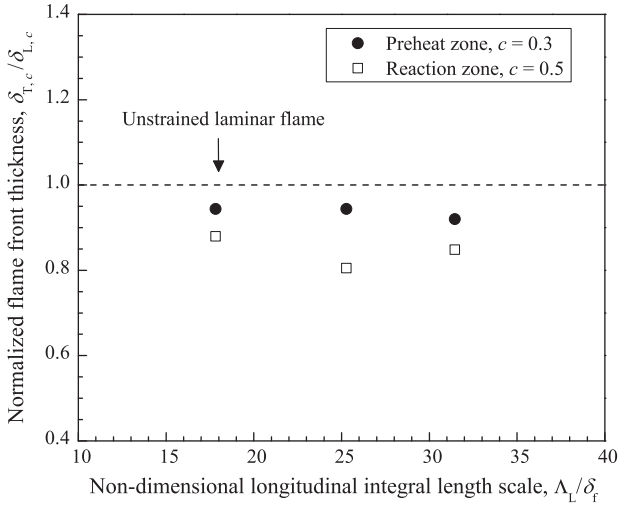

Fig. 18. Normalized preheat zone and reaction zone thicknesses as a function of the non-dimensional longitudinal integral length scale for the third set of experiments.

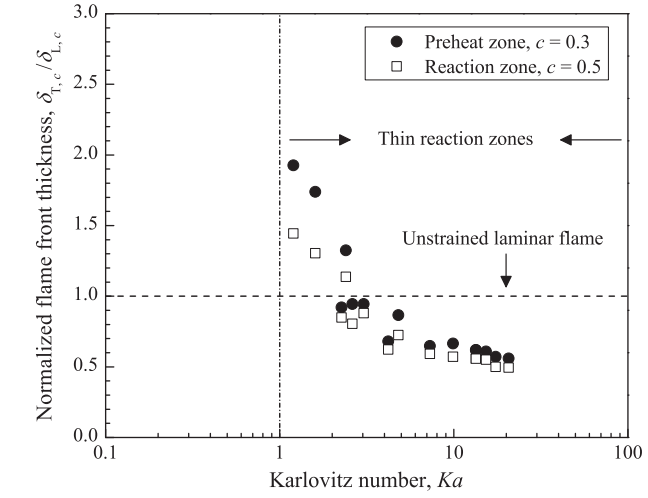

Fig. 19. Normalized preheat zone and reaction zone thicknesses as a function of the Karlovitz number for all three sets of experiments.

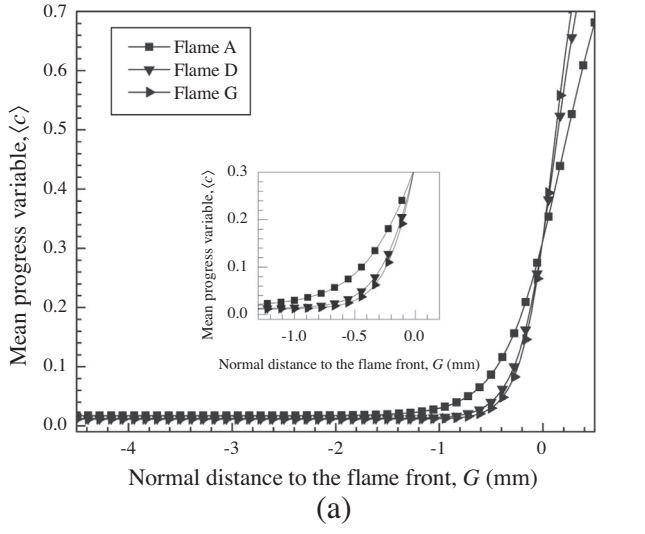

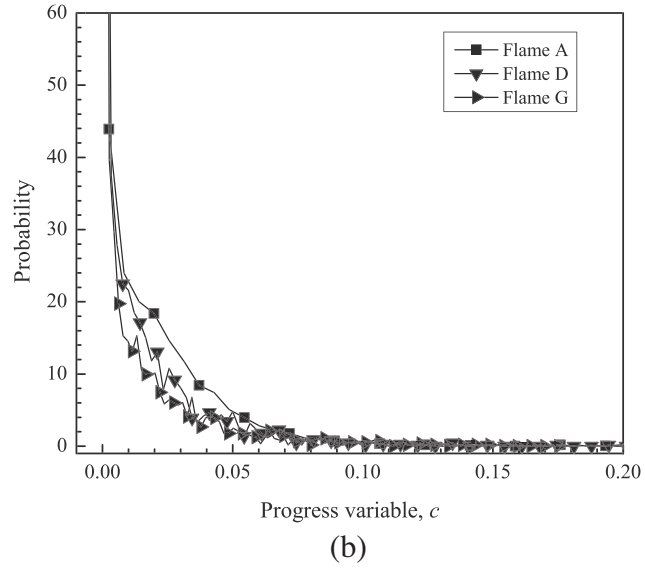

Fig. 20. (a) Averaged progress variable profiles normal to the flame fronts, and (b) probability density functions of the progress variable in front of the preheat layers at $G = -2$ mm for Flames A, D, and G.

The normalized preheat zone and reaction zone thicknesses for all three sets of experiments are summarized in Fig. 19. The normalized thicknesses decrease significantly by increasing the Karlovitz number, suggesting that the stretch factor is the dominant mechanism in changing the inner structure of methane/air flame fronts for the conditions studied in this work.

The averaged progress variable profiles for Flames A, D, and G, were calculated using three thousand instantaneous progress variable profiles normal to the flame fronts, Fig. 20(a). The progress variable gradient at $G = 0$ increases as the non-dimensional turbulence intensity is increased from 5.5 to 16.5. This observation reconfirms the reduction of flame front thickness with increasing non-dimensional turbulence intensity previously reported in Fig. 12. The probability density functions of the progress variable in front of the preheat layers at $G = -2$ mm are shown in Fig. 20(b). These distributions seem to be insensitive to an increase in the non-dimensional turbulence intensity. This observation implies that for ultra-lean conditions the scalar structure in front of the preheat layers seems to stay unchanged and not affected significantly by the turbulent structures that may be preheated by the reaction layers in the thin reaction zones regime.

5. Concluding remarks

The preheat zone and reaction zone thicknesses of premixed turbulent methane/air flames stabilized on a Bunsen-type burner using a premixed ethylene/air pilot flame were investigated. Particle image velocimetry and Rayleigh scattering techniques were used to measure the instantaneous velocity and temperature fields, respectively. All experimental conditions are mainly located in the thin reaction zones regime since all Karlovitz numbers are greater than unity.

It was observed that the shapes of probability density functions for the normalized preheat zone and reaction zone thicknesses were similar to a log-normal distribution. The normalized preheat zone and reaction zone thicknesses decreased with increasing non-dimensional turbulence intensity in ultra-lean premixed turbulent flames at an equivalence ratio of 0.6, and these normalized thicknesses were observed to be less than unity. The preheat zone and reaction zone thicknesses of strained premixed laminar flames and premixed turbulent flames at zero-curvature flame fronts had a similar behavior and decayed exponentially by increasing the Karlovitz number. In addition, the measured preheat zone and reaction zone thicknesses were found to become larger by increasing the local flame front curvature. The amount of flame front thickening was equally distributed between the positive and negative curvatures.

The normalized preheat zone and reaction zone thicknesses increased for equivalence ratios varying from 0.6 to 1.0 under a constant bulk flow velocity. These normalized thicknesses were less than unity for equivalence ratios of 0.6 and 0.7, whereas they were higher than unity for equivalence ratios varying from 0.8 to 1.0. It was discussed that the formation of thick flame fronts may not be due to the penetration of Kolmogorov-scaled structures into the flame fronts since the mean widening for progress variable contours of premixed turbulent flames in comparison with corresponding values of unstrained premixed laminar flames was insignificant. However, the creation of thick flame fronts may be attributed to the overestimation of flame front thickness due to the 2D image processing.

The normalized preheat zone and reaction zone thicknesses were insensitive to the non-dimensional longitudinal integral length scale. These normalized thicknesses were less than unity, indicating that the thin laminar flamelet assumption is valid for these experimental conditions.

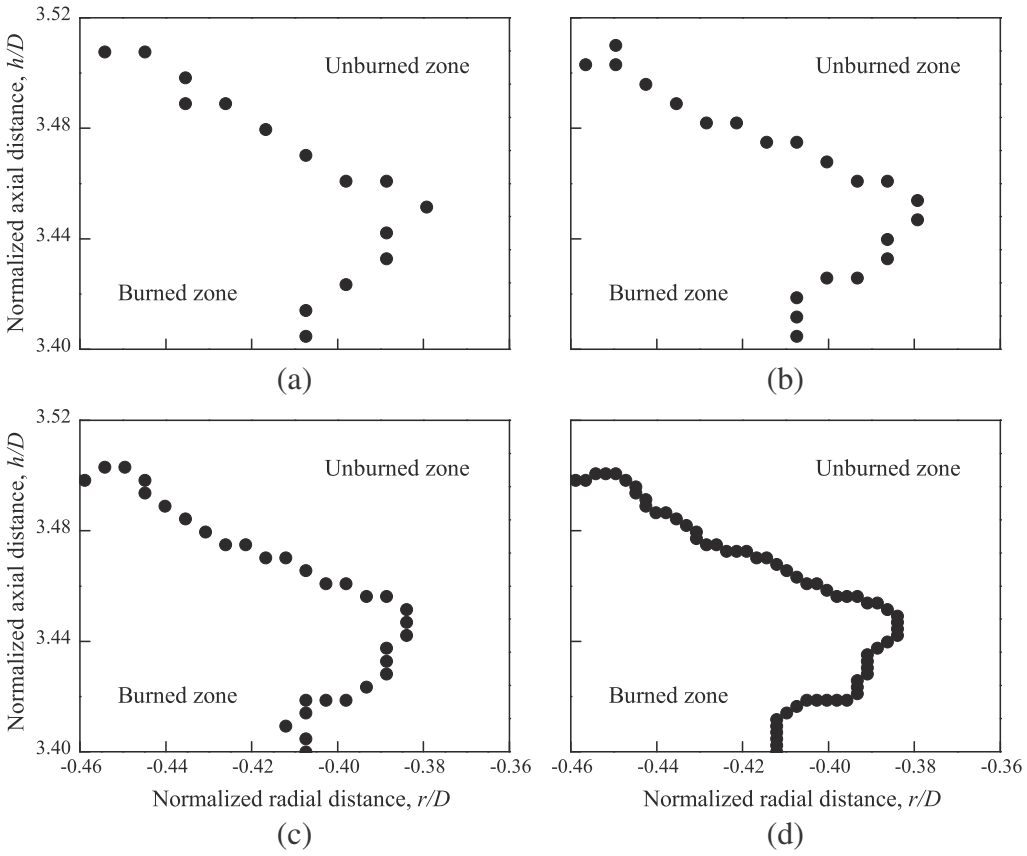

Fig. A.1. Instantaneous flame front conditioned at $c = 0.3$ for a magnification ratio of (a) 4.8, (b) 6.4, (c) 9.6, and (d) 19.2 pixels/mm for Flame B.

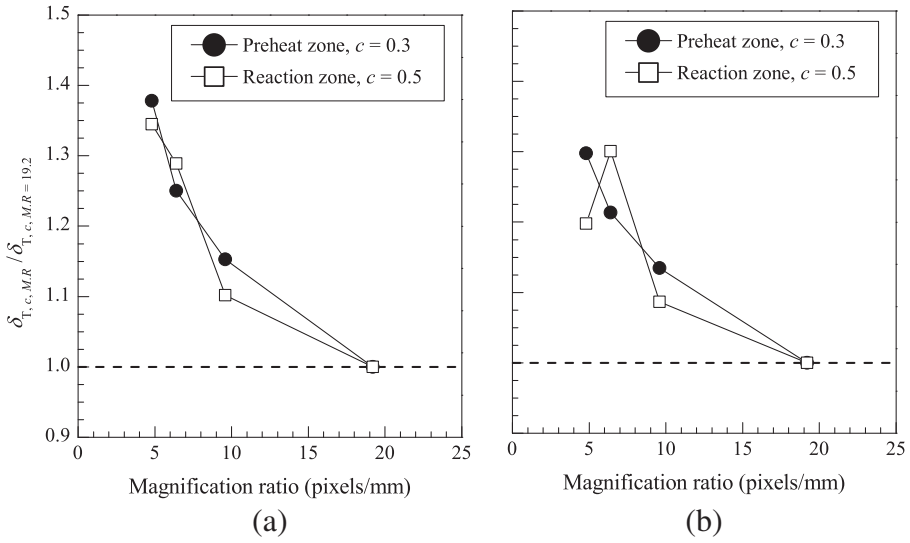

Fig. A.2. Preheat zone and reaction zone thicknesses normalized by the corresponding values at the magnification ratio of 19.2 pixels/mm for (a) Flame B, and (b) Flame G.

The normalized preheat zone and reaction zone thicknesses decreased by increasing the Karlovitz number, implying that the thinning of the flame front thickness is dominated by the total stretch rate.

Acknowledgment

The financial support from the Natural Sciences and Engineering Research Council of Canada (NSERC) is gratefully acknowledged.

Appendix A. Effect of the magnification ratio

The influence of reduced magnification ratio on the preheat zone and reaction zone thicknesses is investigated by degrading the magnification ratio for two select conditions, that is, Flames B and G. For each flame condition, the magnification ratio was decreased to 4.8, 6.4, and 9.6 pixels/mm, that is, 208, 156, and 104 μm per pixel. This was done by selecting 4×4, 3×3, and 2×2 pixels^2 from the actual temperature measurement pixels and taking an average over the temperatures within each box. The effect of reduced magnification ratio on an instantaneous flame front conditioned at $c = 0.3$ is shown in Fig. A.1.

The preheat zone and reaction zone thicknesses were then estimated for these reduced magnification ratio conditions. These thicknesses normalized by the corresponding values at the magnification ratio of 19.2 pixels/mm with respect to the magnification ratio for Flames B and G are shown in Fig. A.2. It is shown that for magnification ratios of 4.8 and 6.4 pixels/mm, these thicknesses are about 20–35% higher than the measured thicknesses at 19.2 pixels/mm. This overestimation was expected due to the limited number of pixels across the flame fronts at these low magnification ratios. This states that at these magnification ratios, that is, 4.8 and 6.4 pixels/mm, the flame front thickness is not resolved accurately. However, by increasing the magnification ratio to 9.6 pixels/mm, the differences between the results at this ratio and the measured values at 19.2 pixels/mm are changing from 8% to 15%. It is observed that these thicknesses are converged to the measured values by increasing the magnification ratio to the original condition of 19.2 pixels/mm, and after the magnification ratio is 15 pixels/mm, the variation of these thicknesses with the magnification ratio is insignificant. This implies that the magnification ratio of the current experimental setup is sufficient to resolve the flame front thickness properly.

References

[1] N. Peters, Proc. Combust. Inst. 21 (1986) 1231–1250.
[2] T. Poinsot, D. Veynante, S. Candel, Proc. Combust. Inst. 23 (1990) 613–619.
[3] N. Peters, J. Fluid Mech. 384 (1999) 107–132.
[4] V.L. Zimont, Combust. Explo. Shock Waves 15 (1979) 305–311.
[5] P.D. Ronney, V. Yakhot, Combust. Sci. Technol. 86 (1992) 31–43.
[6] M.S. Mansour, N. Peters, Y.C. Chen, Proc. Combust. Inst. 27 (1998) 767–773.
[7] F. O'Young, R.W. Bilger, Combust. Flame 109 (1997) 682–700.
[8] R. Sankaran, E.R. Hawkes, J.H. Chen, T. Lu, C.K. Law, Proc. Combust. Inst. 31 (2007) 1291–1298.
[9] F.T.C. Yuen, Ö.L. Gülder, Proc. Combust. Inst. 32 (2009) 1747–1754.
[10] J.F. Driscoll, Prog. Energy Combust. Sci. 34 (2008) 91–134.
[11] A. Buschmann, F. Dinkelacker, T. Schäfer, M. Schäfer, J. Wolfrum, Proc. Combust. Inst. 26 (1996) 437–445.
[12] A. Soika, F. Dinkelacker, A. Leipertz, Proc. Combust. Inst. 27 (1998) 785–792.
[13] D. Most, V. Höller, A. Soika, F. Dinkelacker, A. Leipertz, in: R.J. Adrian et al. (Eds.), Laser Techniques Applied to Fluid Mechanics, Springer, Berlin-Heidelberg, 2000, pp. 505–519.
[14] L.P.H. de Goey, T. Plessing, R.T.E. Hermanns, N. Peters, Proc. Combust. Inst. 30 (2005) 859–866.
[15] D. Thévenin, Proc. Combust. Inst. 30 (2005) 629–637.
[16] F. Dinkelacker, Experimental validation of flame regimes for highly turbulent premixed flames, in: Proceedings of the European Combustion Meeting, Orléans, France, 2003, pp. 158–163.
[17] C. Kortschik, T. Plessing, N. Peters, Combust. Flame 136 (2004) 43–50.
[18] F.T.C. Yuen, Ö.L. Gülder, AIAA J. 47 (2009) 2964–2973.
[19] Spectra-Physics, Quanta-Ray Lab-Series Lasers: Pulsed Nd:YAG Lasers, User's Manual, 2003.
[20] G.H. Wang, N.T. Clemens, Exp. Fluids 37 (2004) 194–205.
[21] D. Goodwin, N. Malaya, H.K. Moffat, R. Speth, Cantera. <http://code.google.com/p/cantera/>.
[22] G.P. Smith, D.M. Golden, M. Frenklach, N.W. Moriarty, B. Eiteneer, M. Goldenberg, C.T. Bowman, R.K. Hanson, S. Song, W.C. Gardiner, V.V. Lissianski, Z. Qin, GRI-Mech 3.0. <http://www.me.berkeley.edu/gri_mech/>.
[23] N. Peters, Turbulent Combustion, Cambridge University Press, Cambrdige, 2000.
[24] Y.C. Chen, R.W. Bilger, Exp. Therm. Fluid Sci. 27 (2003) 619–627.
[25] P. Griebel, P. Siewert, P. Jansohn, Proc. Combust. Inst. 31 (2007) 3083–3090.
[26] G.K. Batchelor, The Theory of Homogeneous Turbulence, Cambridge University Press, 1953.
[27] R. Borghi, in: C. Casci, C. Bruno (Eds.), Recent Advances in Aerospace Sciences, Plenum Press, New York, 1985, pp. 117–138.
[28] J.A. Sutton, J.F. Driscoll, Opt. Lett. 29 (2004) 2620–2622.
[29] D.A. Knaus, S.S. Sattler, F.C. Gouldin, Combust. Flame 141 (2005) 253–270.
[30] I.G. Shepherd, R.K. Cheng, T. Plessing, C. Kortschik, N. Peters, Proc. Combust. Inst. 29 (2002) 1833–1840.
[31] F. Dinkelacker, A. Soika, D. Most, D. Hoffmann, A. Leipertz, W. Polifke, K. Döbbeling, Proc. Combust. Inst. 27 (1998) 857–865.

[32] F.T.C. Yuen, Ö.L. Gülder, Proc. Combust. Inst. 34 (2013) 1393–1400.
[33] B. Karlovitz, D.W. Denniston, D.H. Knapschaefer, F.E. Wells, Proc. Combust. Inst. 4 (1953) 613–620.
[34] S.M. Candel, T.J. Poinsot, Combust. Sci. Technol. 70 (1990) 1–15.
[35] F. Mokhtarian, A. Mackworth, IEEE Trans. Pattern Anal. Mach. Intell. 8 (1986) 34–43.
[36] F. Halter, C. Chauveau, I. Gökalp, Combust. Sci. Technol. 180 (2008) 713–728.
[37] N. Darabiha, S.M. Candel, F.E. Marble, Combust. Flame 64 (1986) 203–217.
[38] C.J. Sung, J.B. Liu, C.K. Law, Combust. Flame 106 (1996) 168–183.
[39] H.N. Najm, P.S. Wyckoff, Combust. Flame 110 (1997) 92–112.

Please cite this article in press as: P. Tamadonfar, Ö.L. Gülder, Combust. Flame (2014), http://dx.doi.org/10.1016/j.combustflame.2014.07.001